Supporting Information

Aligned Vertical Mass Transfer Channels in 2D Monolayered Fe−N−C Carbon Honeycomb for Efficient Oxygen Reduction

Mian He,[a] Yaqi Zhang,[a] Jiali Lou,[a] Jiamin Wei,[ab] Xuhui Sun,[c] Meng An,*[c] Shenghua Zhou,[a] Xiaoqian Wei,*[de] and Xiaokai Song,*[a]

[a] *The Jiangsu Key Laboratory of Clean Energy Storage and Conversion, School of Chemistry and Chemical Engineering, Jiangsu University of Technology, Changzhou 213001, China*

[b] Key Laboratory of Advanced Catalytic Materials and Technology, Advanced Catalysis and Green Manufacturing Collaborative Innovation Center, Changzhou University, Changzhou 213164, China.

[c] *Yangtze Delta Region Academy in Jiaxing, Beijing Institute of Technology, Jiaxing 314019, China*

[d] *Faculty of Science and Engineering, Waseda University, Tokyo 169-0051, Japan*

[e] *Department of Materials Process Engineering, Graduate School of Engineering, Nagoya University, Furo-cho, Chikusa-ku, Nagoya, Aichi 464-8603, Japan.*

*Corresponding author.

E-mail address: anmeng@sust.edu.cn (M. An), xqwei@akane.waseda.jp (X. Wei),

xksong@jsut.edu.cn (X. Song).

1. Experimental Section

1.1 Chemicals and materials

2-methylimidazole (98%) and Nafion (5 wt. % in lower aliphatic alcohols and water, contains 15-20% water; Nafion 1100EW) were purchased from Energy Chemical Co., Ltd. and Sigma-Aldrich, respectively. Other reagents and solvents were purchased from Sinopharm Co. Ltd. and used without further purification. Deionized (DI) water with resistivity higher than 18 MΩ cm was used during the experiments.

1.2 Synthesis of ZIF-8 nanoparticle and derived carbon catalysts

Truncated rhombic dodecahedral ZIF-8. Typically, a 25 mL aqueous solution of $Zn(CH_3COO)_2 \cdot 2H_2O$ (1.50 g, 6.8 mmol) was prepared and added to a vigorously stirred 25 mL aqueous solution containing 2-methylimidazole (5.60 g, 68 mmol) and cetyltrimethylammonium bromide (CTAB) (5.0 mg, 0.014 mmol). The resulting mixture was then aged undisturbed at room temperature for 2 h. The precipitated crystals were collected by centrifugation, washed thoroughly with DI water. The yield of ZIF-8 was determined gravimetrically from the mass of the dried product and used to prepare a colloidal dispersion of ZIF-8 at the target concentration for subsequent synthesis steps.

Fe^{3+}/ZIF-8/urea hybrid structures (Fe^{3+}/ZIF-8/urea-*n*, *n* represents the dosage of urea), Fe^{3+}/ZIF-8 and ZIF-8/urea-75 hybrid structures. Fe^{3+}/ZIF-8/urea-75 was synthesized via an ice-templating-assisted coassembly strategy. Typically, 300 mg of as-prepared ZIF-8, 75 mg of urea, and 0.2 mg of $FeCl_3$ were dispersed in 30 mL of DI water and subjected to ultrasonication for 30 min to yield a homogeneous colloidal dispersion. The resulting suspension was immersed gradually into liquid nitrogen for 5 min to ensure complete directional freezing of the aqueous phase into ice crystals. Subsequently, the frozen monolith was lyophilized for 24 h to remove the ice template, affording the porous Fe^{3+}/ZIF-8/urea-75 architecture. Analogously, Fe^{3+}/ZIF-8/urea-50, Fe^{3+}/ZIF-8/urea-100, and Fe^{3+}/ZIF-8 (urea-free) were prepared using identical protocol with urea mass varied to 50 mg, 100 mg, and 0 mg, respectively. For comparative purposes, the ZIF-8/urea-75 hybrid ($FeCl_3$-free) was synthesized under otherwise identical conditions.

1.3 Synthesis of 2D carbon-based catalysts

2D monolayered Fe−N−C carbon honeycomb catalysts (2D Fe-CH-*n*), 2D monolayered Fe−N−C carbon particle array catalyst (2D Fe-CPA), and 2D monolayered N−C carbon honeycomb catalyst (2D CH-75). 2D Fe-CH-*n*, 2D Fe-CPA, and 2D CH-75 were prepared by a high-temperature pyrolysis of hybrid precursors under inert atmosphere. Typically, a sample of 300 mg of Fe^{3+}/ZIF-8/urea-*n* (Fe^{3+}/ZIF-8/urea-50, Fe^{3+}/ZIF-8/urea-75, and Fe^{3+}/ZIF-8/urea-100), Fe^{3+}/ZIF-8 or ZIF-8/urea-75 was first calcined at 500 °C for 2 hours, then the temperature was increased to 900 °C with a heating rate of 3 °C min^{-1}, and kept for 2 hours. After natural cooling to room temperature, the catalyst was collected and designated as 2D Fe-CH-50, 2D Fe-CH-75, 2D Fe-CH-100, 2D Fe-CPA, and 2D CH-75, respectively.

1.4 Materials characterization

The morphology and chemical composition of the samples were investigated by scanning electron microscopy (SEM, Hitachi S-3400N) and transmission electron microscopy (TEM, JEOL JEM-2100). The surface chemistry was analyzed by X-ray photoelectron spectroscopy (XPS) performed on a AXISULTRA DLD XPS System with

MONO Al source and the binding energies were calibrated using the C 1s peak at 284.8 eV. The phase composition of samples was investigated by X-ray diffraction (XRD, PANalytical X' Pert Powder). All measurements were performed at room temperature and atmospheric pressure. Brunauer–Emmett–Teller (BET) surface area of all samples was measured by N_2 adsorption and desorption at 77 K using a AUTOSORB system. The samples were degassed offline at 200 °C for 10 h under vacuum before the analysis. And the pore size distribution was analyzed by NLDFT Advanced PSD. Raman measurements were conducted at room temperature on a Horiba Jobin-Yvon LabRAM HR800 spectrometer. The X-ray absorption spectroscopy (XAS) measurements were obtained on the Beam line BL14W1 and BL11B at the Shanghai Synchrotron Radiation Facility (SSRF).

1.5 Electrochemical measurements

The electrochemical measurements of ORR performance were tested on a CHI760E electrochemical workstation in a conventional three-electrode system at room temperature. Catalyst ink was prepared by dispersing 5 mg of catalyst in a mixed solution containing 960 μL of ethanol and 40 μL of 5 wt% Nafion solution by ultrasonication to obtain a homogeneous suspension. The electrolytes were composed of 0.1 M KOH. An Ag/AgCl (3M KCl) electrode and a carbon rod were used as reference and counter electrode, respectively. The experiments were conducted at room temperature and all of the potentials were calibrated to a reversible hydrogen electrode (RHE). Generally, a RDE electrode with a diameter of ϕ 3 mm was used as the substrate for the working electrode. An aliquot of 8 μL of the catalyst ink was loaded onto the working electrode and dried under ambient conditions with a mass loading of 0.57 mg cm^{-2}. The electrolyte was purged by a specific gas for at least 30 min before the measurements and the gas flow was maintained during the experiments. Cyclic voltammetry (CV) measurements were conducted at a scan rate of 50 mV s^{-1} and a rotation rate of 1600 rpm. To eliminate the influence of background current, the linear scan voltammetry (LSV) measurements were recorded at a scan rate of 1 mV s^{-1}. The double-layer capacitance (C_{dl}) was measured by a series of CV scanning in a non-Faradaic potential at various scan rates of 5-60 mV s^{-1} in N_2-saturated 0.1 M KOH. The EIS test was carried out from 10^5 Hz to 10^{-2} Hz and recorded at OCP with an amplitude of 10 mV. The tolerance of the electrocatalysts to methanol poisoning was evaluated by injecting 5 mL of 3 M methanol into the electrolyte (150 mL) during the chronoamperometric measurements. For comparison, Pt/C (20 wt% platinum, JM) was conducted on the same electrochemical tests.

To obtain the electron transfer number (n) and hydrogen peroxide yield (% H_2O_2), a rotating ring disk electrode (RRDE) electrode (diameter: ϕ 4 mm) served as working electrode. The catalyst ink (12 μL) was dropped on the RRDE electrode and then dried in the air. The % H_2O_2 and n were calculated as the following equations:

$$\%H_2O_2 = 200 \times \frac{I_R/N}{I_D + I_R/N} \quad (1)$$

$$n = \frac{4}{1 + \frac{I_R}{I_D} \times N} \quad (2)$$

Where I_D and I_R are the disk and ring currents, respectively, and N is the collection efficiency (37%) of the ring electrode.

The rotating speed of RDE was controlled from 400 to 2025 rpm. The Koutecký-Levich equation is:

$$\frac{1}{j} = \frac{1}{j_L} + \frac{1}{j_K} = \frac{1}{B\omega^{1/2}} + \frac{1}{j_K} \quad (3)$$

$$B = 0.62nFC_0(D_0)^{2/3}\nu^{-1/6} \quad (4)$$

$$j_K = nFkC_0 \quad (5)$$

Where j is the measured current density, j_K and j_L are the kinetic- and diffusion-limiting current densities, ω is the angular velocity of the disk ($\omega = 2\pi N$, N is the linear rotation speed), n represents the overall number of electrons transferred in oxygen reduction, F is the Faraday constant (F = 96485 C mol^{-1}), C_0 is the bulk concentration of O_2 (1.2×10^{-6} mol cm^{-3}), D_0 is the diffusion coefficient of O_2 in 0.1 M KOH electrolyte (1.9×10^{-5} cm^2 s^{-1}), v is the kinematic viscosity of the electrolyte (0.01 cm^2 s^{-1}), and k is the electron transfer rate constant.

1.6 Zinc air batteries (ZABs) measurement

1.6.1 Liquid ZABs

Liquid ZABs were assembled in a typical two electrode configuration, in which a metallic zinc foil of purity ~99.9% and an air electrode were used as anode and cathode, respectively. The air electrode used a carbon paper-based gas diffusion layer (TORAY-YLS 30T). The catalyst ink was drop casted onto the gas diffusion layer and dried by a hot air gun (temperature set at 80 °C). The catalyst loading was controlled to 1.0 mg cm^{-2}. The electrolyte was aqueous 6 M KOH with 0.2 M zinc acetate, which was constantly purged with pure oxygen at a rate of 40 mL min^{-1}. Prior to performance tests, the electrolyte was also purged with oxygen for 30 min in order to saturate electrolyte with oxygen. The open circuit voltage, discharging and charging polarization curves were recorded using the CHI760E electrochemical workstation. Rate performance of the assembled ZABs were evaluated by recording voltage profiles during galvanostatic discharge at various current densities from 5 to 50 mA cm^{-2}. The constant current discharge-charge cycle curves and specific capacity of the batteries were carried out at room temperature using a battery test system (Land 3001A). The ZABs were discharged for 150 second and charged for 150 second at a current density of 10 mA cm^{-2} in each galvanostatic cycle. The specific capacity and energy density were calculated according to the following equations:

$$\text{Specific capacity (mAh}\cdot g^{-1}) = I \times t/w_{Zn} \quad (6)$$

where I is the applied current (A), t is the serving time (s), V is the average discharge voltage (V), and w_{Zn} is the weight of zinc consumed (g).

1.6.2 Flexible ZABs

Flexible solid-state ZAB is consisted of air electrode, polyacrylic acid (PAA) film and zinc foil, which were served as air electrode, solid electrolyte and anode, respectively. The air electrode consists of a piece of nickel foam (NF) on the air-facing side as the current collector, a gas diffusion layer (GDL) in the middle, and a carbon cloth layer coated with catalyst (catalyst loading of 1.0 mg cm^{-2}) on the electrolyte-facing side. To prepare PAA gel electrolyte: 1 g of *N*, *N*-methylene diacrylamide as a cross-linker and 5 g of acrylic acid were quickly poured into 20 mL of DI water containing 18 g of KOH under continuous stirring, followed by dissolving 1.5 g of zinc acetate. After stirring for 2 h, $K_2S_2O_8$ aqueous solution (0.12 g dissolved in 20 mL of DI water) as the initiator was added to the aforementioned solution in the square mold and then shaken vigorously to form the PAA gel. The polarization curves were recorded via linear sweep voltammetry (LSV) at room temperature on a CHI 760E electrochemical working station. Both the current density and power density were normalized to the effective surface area of the air electrode. The ZABs were discharged for 150 second and charged for 150 second at a current density of 1 mA cm^{-2} in each galvanostatic cycle.

1.7 Finite element calculation

To investigate the electrolyte diffusion across two-dimensional (2D) arrayed nanoparticles with various

configurations, the flux velocity and pressure distribution of electrolyte were calculated using finite element calculations. One cube nanoparticle with a side length of 200 nm and a chamfer of 35 nm was constructed as the basic unit of the self-assembly catalyst. For 2D Fe-CPA, we constructed an ordered permutation of 6×10 basic units and applied periodic boundary conditions in two in-plane directions to simulate an infinitely large 2D plane. For 2D-Fe-CH-75, the cube nanoparticle with side length of 200 nm was wrapped in the hexagonal lattice with side length of 400 nm. The mass diffusion behavior of electrolytes across microporous catalyst with two configurations was modeled utilizing finite element analysis. The fluid motion inside the microporous structure was described by Navier-Stoke equation:

$$\rho\frac{\partial u}{\partial t} - \nabla \cdot \left[-pI + \mu\left(\nabla u + (\nabla u)^T\right)\right] + \rho u \cdot \nabla u = F \quad (7)$$

$$-\nabla \cdot u = 0 \quad (8)$$

where ρ is the density of solution fluid, $u = (u,v,w)$ is the velocity distribution of fluid, p is the fluid pressure, $\boldsymbol{I}$ is the unit diagonal matrix, η is the fluid viscosity, $\boldsymbol{F} = (f_x, f_y, f_z)$ is the volumetric force. The density and viscosity of solution fluid were set as 1000 kg m^{-3}, u = 0.001 Pa · s. Due to no volumetric force in our simulation system, F =0. Assumed that there is no viscosity in the outlet and inlet,

$$\left[\nabla \cdot \mu\left(\nabla u + (\nabla u)^T\right)\right] \cdot n = 0 \quad (9)$$

$$p = p_i \quad (10)$$

p_i is the pressure at inlet and is set as 10 Pa. Nanoparticles contain numerous porous structures that facilitate the transfer of electrolytes. In our simulations, the nanoparticle was modeled as a porous medium using the porous medium flow model in finite element simulations.

For the catalysis reaction, the mass balance equation describes the accumulation and flux equilibration. For there is no homogeneous reaction, the mass balance of fluid is written as

$$\frac{\partial c_i}{\partial t} + \nabla N_i = 0 \quad (11)$$

where N_i is the flux vector of mass transfer. In our study, we calculated the flux velocity distribution of solution through the internal channels of different geometries particles. For the bulk model, the solution is driven to the flow into the system from three faces with equal normal pressure, and out of the system from the corresponding other three faces. Meanwhile, the periodic boundary condition was set along the direction,

$$u_{src} = u_{drc} \quad (12)$$

$$P_{src} = P_{dst} + \Delta P \quad (13)$$

The subscript of *src* and *dst* are the outlet and inlet of fluid mass transfer when the periodic boundary conditions was applied.

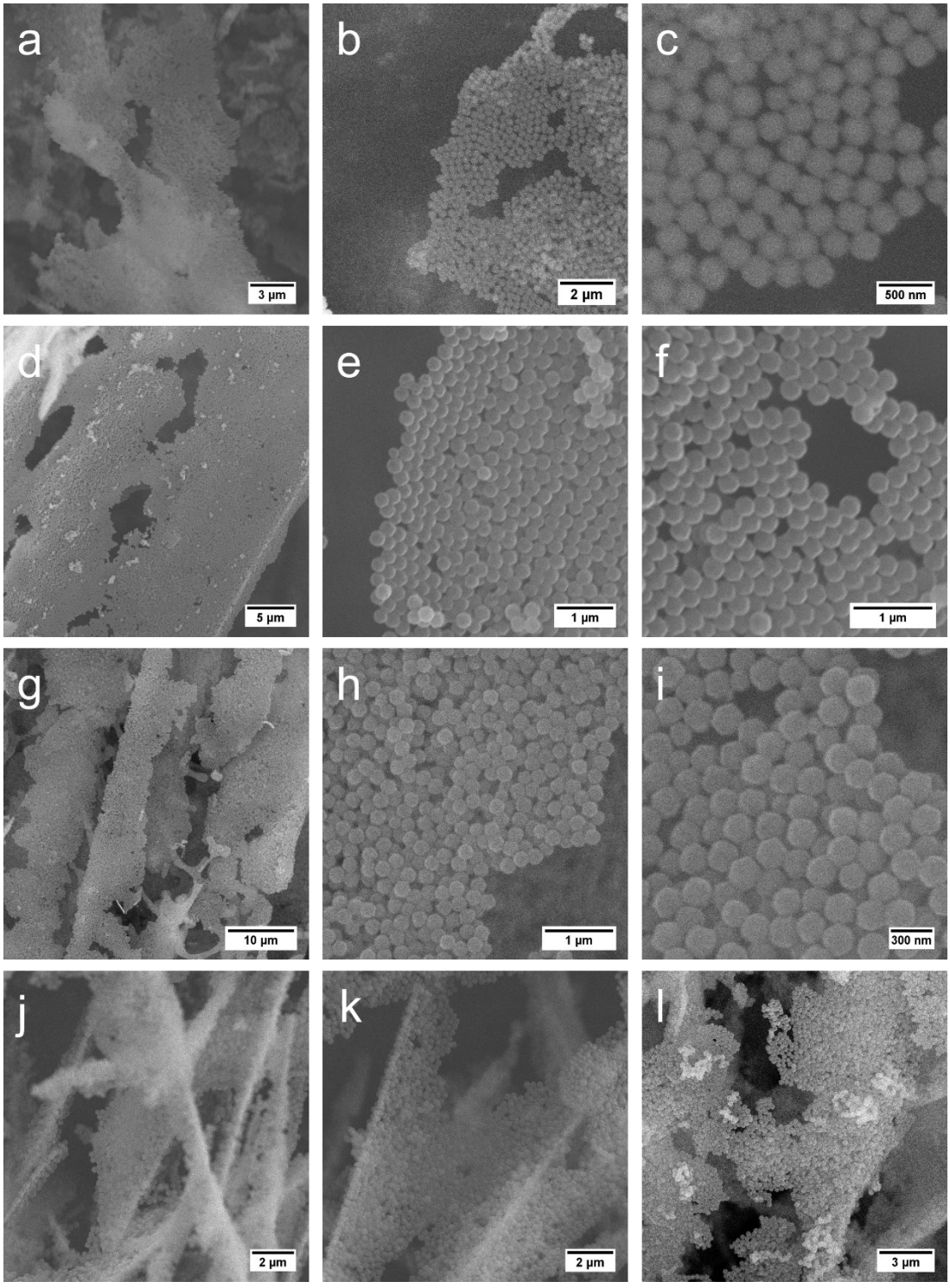

Fig. S1 SEM images of Fe^{3+}/ZIF-8/urea-*n*. (a-c) Fe^{3+}/ZIF-8/urea-50, (d-f) Fe^{3+}/ZIF-8/urea-75, (g-i) Fe^{3+}/ZIF-8/urea-100, and (j-l) Fe^{3+}/ZIF-8.

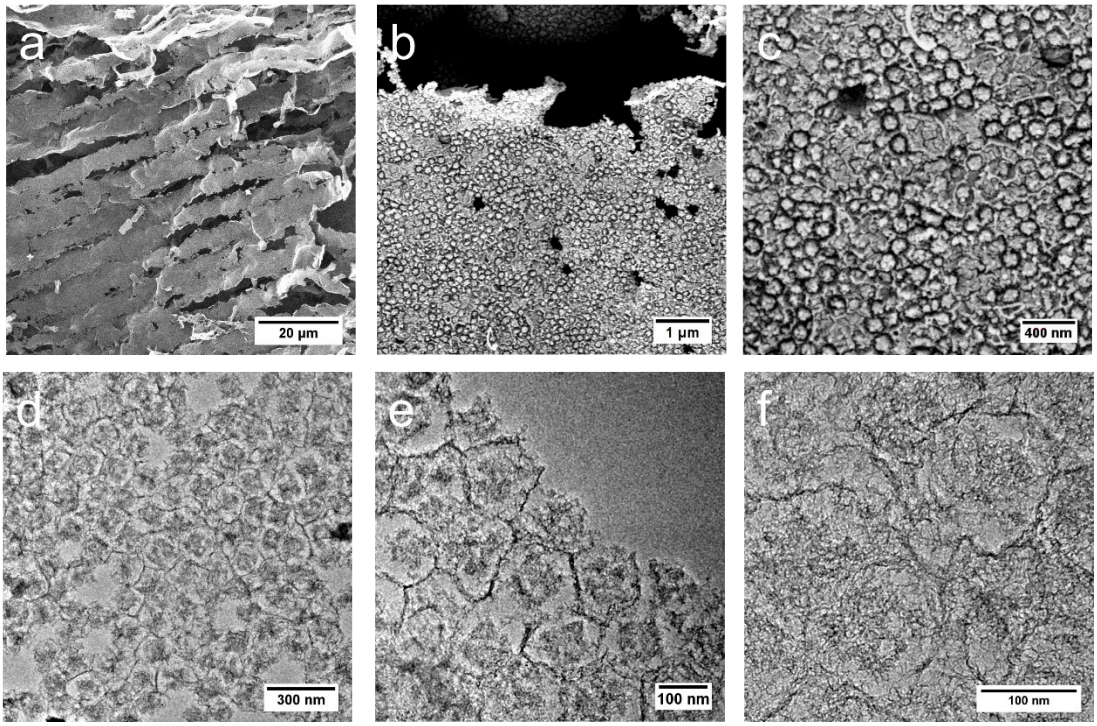

Fig. S2 (a-c) SEM and (d-f) TEM images of 2D Fe-CH-75.

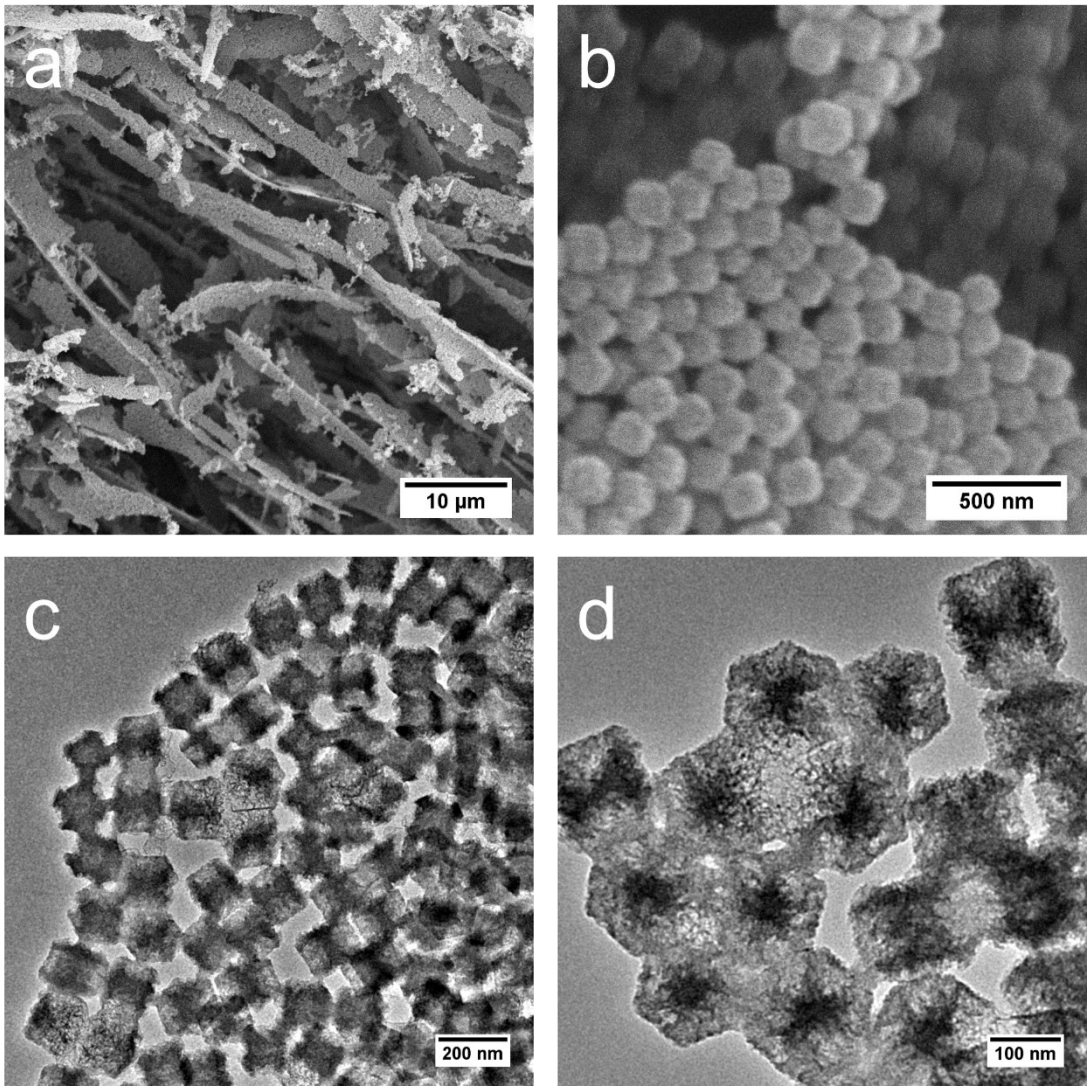

Fig. S3 (a,b) SEM and (c,d) TEM images of 2D Fe-CPA.

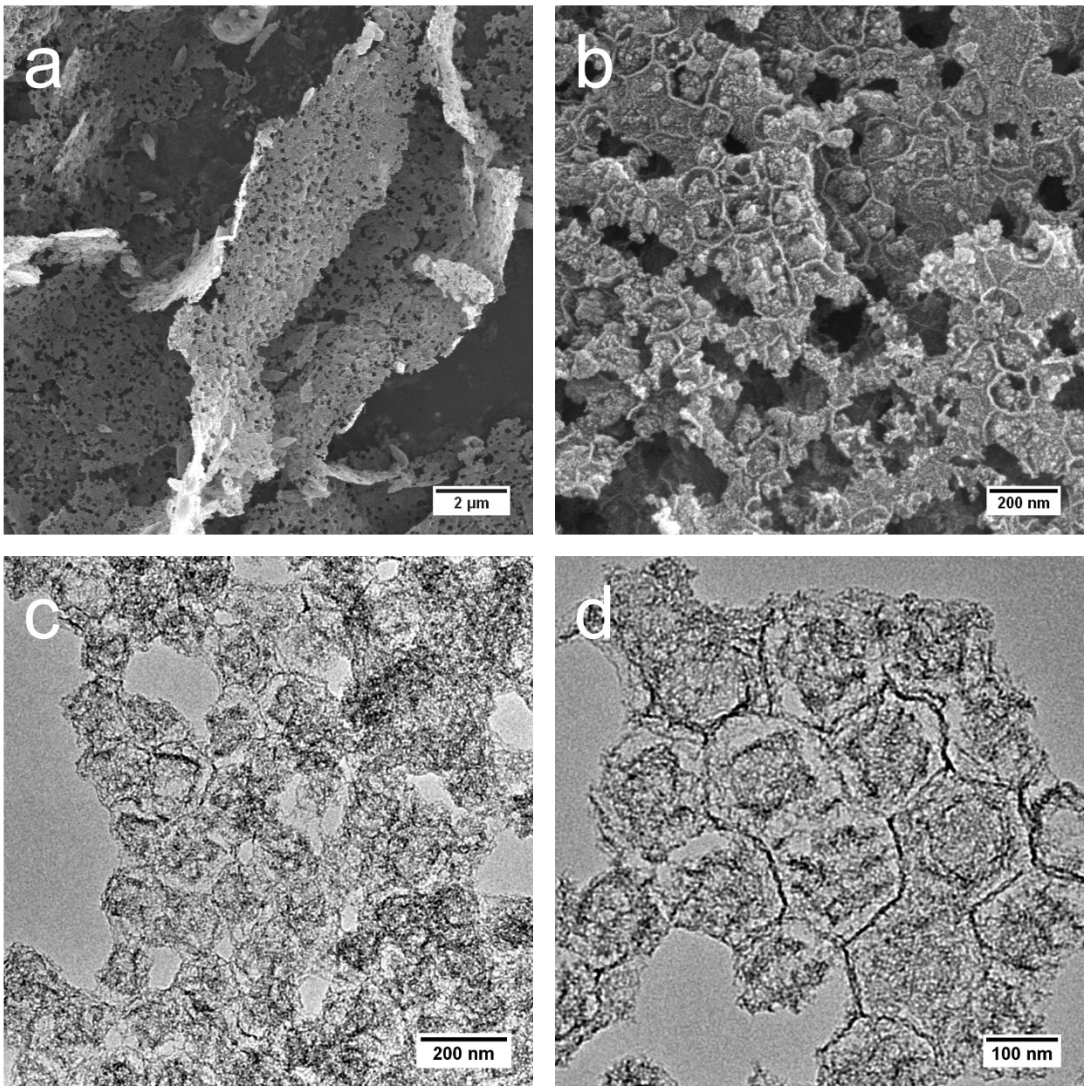

Fig. S4 (a,b) SEM and (c,d) TEM images of 2D Fe-CH-50.

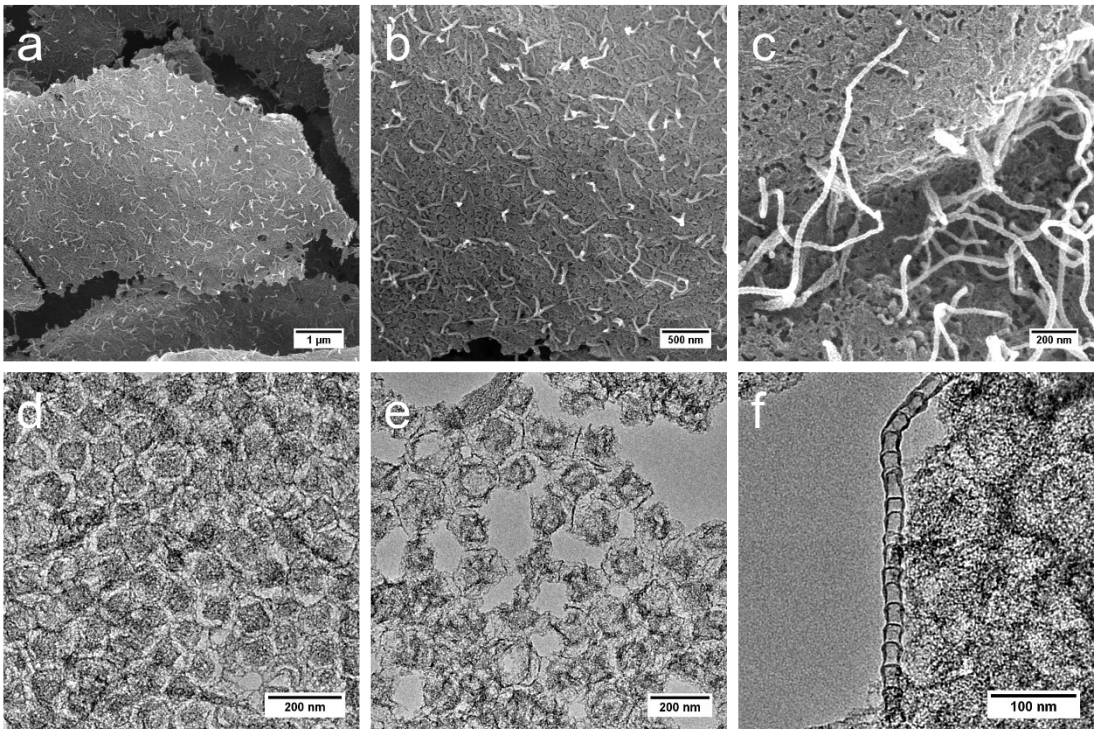

Fig. S5 (a-c) SEM and (d-f) TEM images of 2D Fe-CH-100.

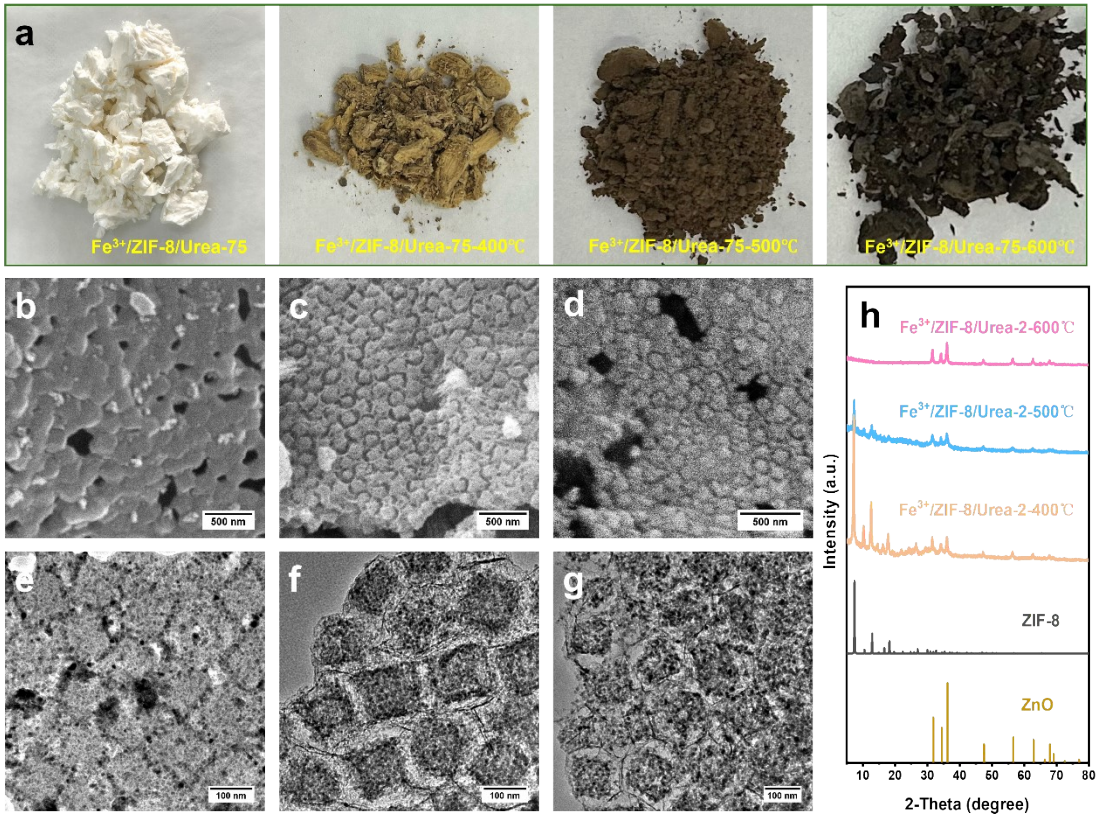

Fig. S6 Illustration of the temperature-dependent pyrolysis of Fe^{3+}/ZIF-8/urea-75. (a) Digital photographs, (b-d) SEM, (e-g) TEM, and (h) XRD patterns of Fe^{3+}/ZIF-8/urea-75-400 °C, Fe^{3+}/ZIF-8/urea-75-500 °C, and Fe^{3+}/ZIF-8/urea-75-600 °C.

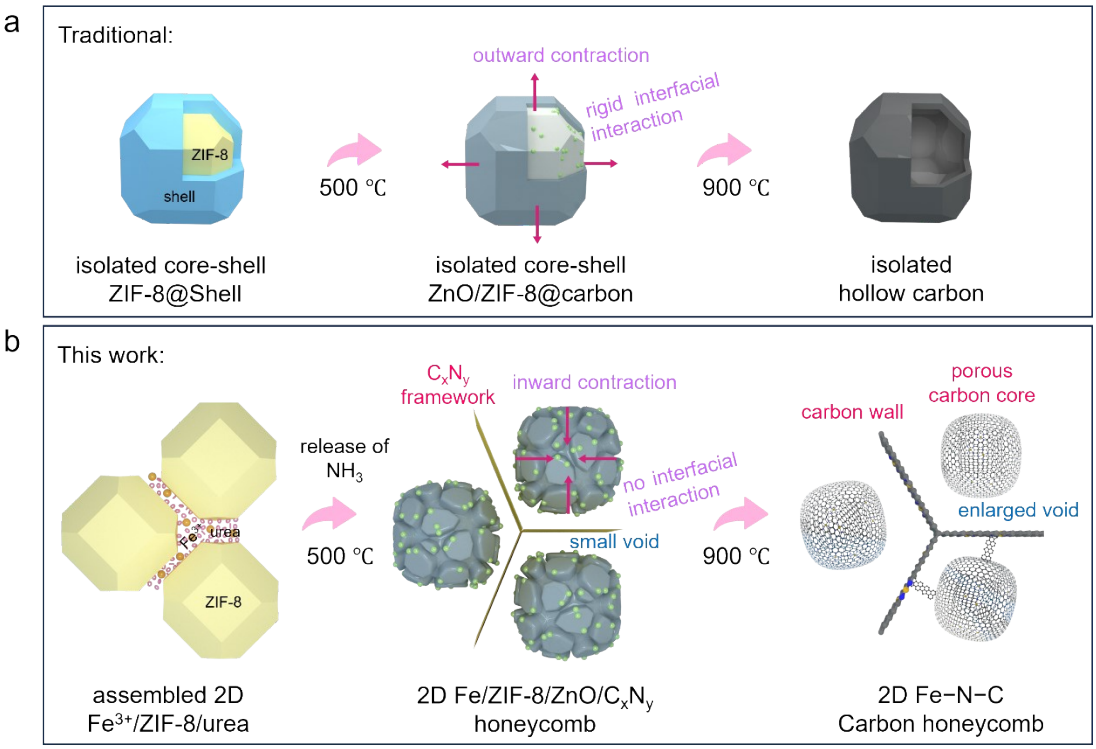

Fig. S7 Schematic illustration of developing mechanism of hollow carbon structure from core-shell ZIF@shell precursors, and (b) 2D carbon honeycomb from assembled hybrid ZIF-8 precursor.

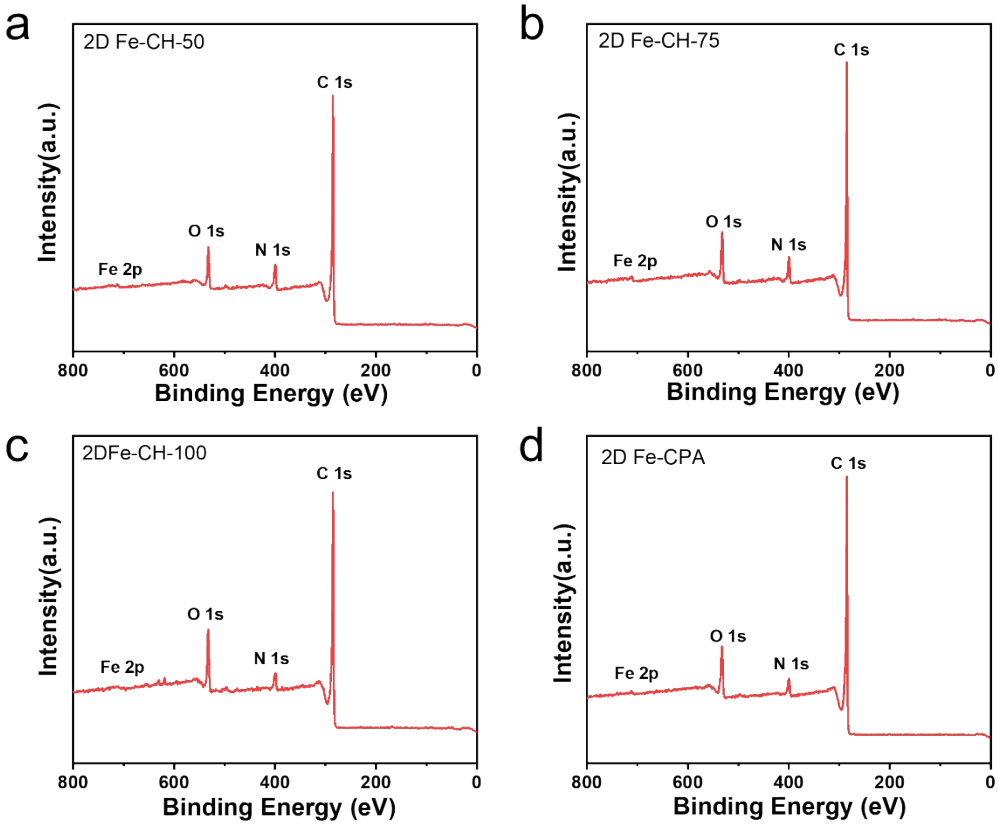

Fig. S8 XPS survey spectra of 2D Fe-CH-50, 2D Fe-CH-75, 2D Fe-CH-100, and 2D Fe-CPA.

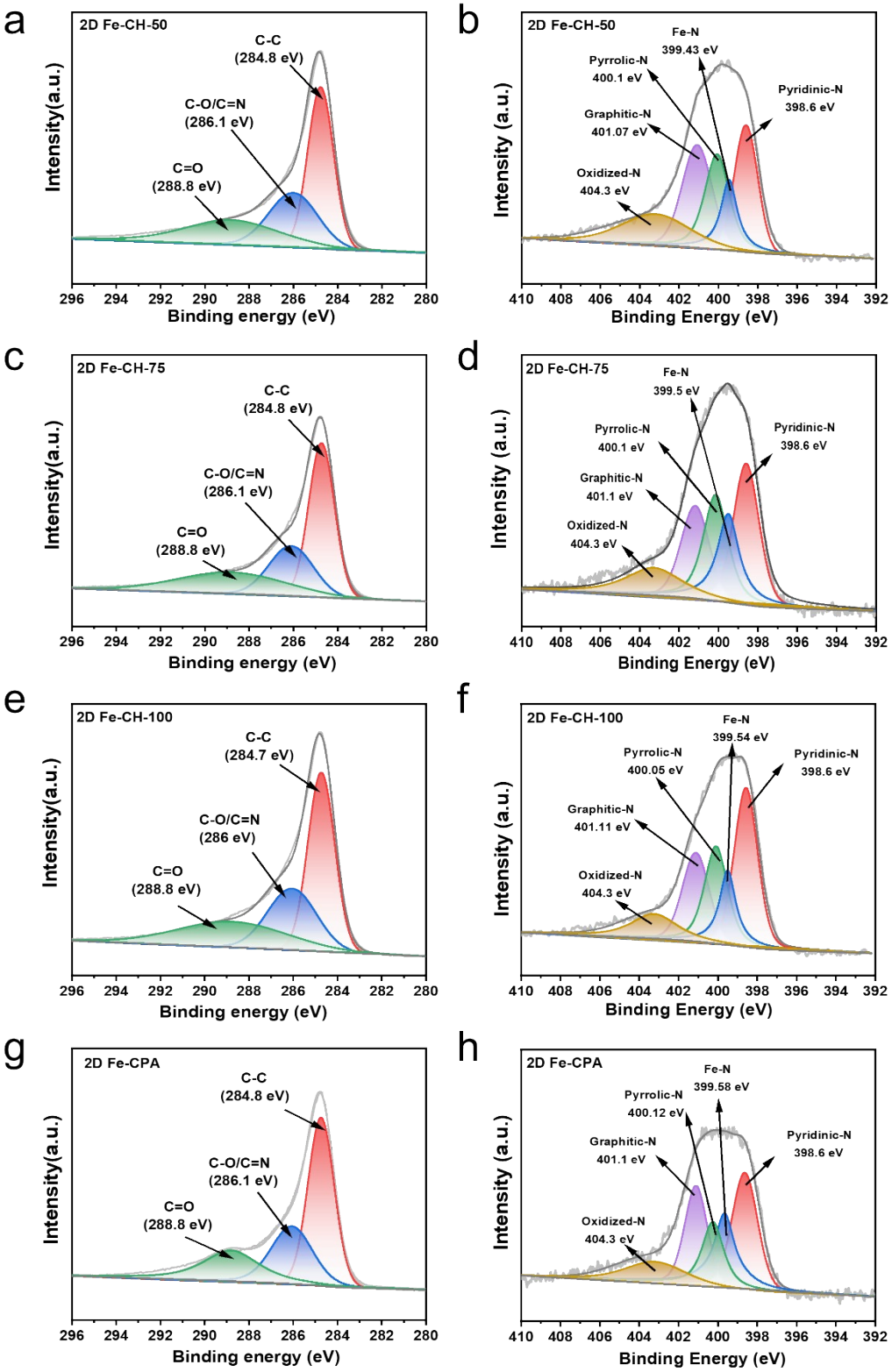

Fig. S9 High-resolution C 1s and N 1s XPS spectra of (a,b) 2D Fe-CH-50, (c,d) 2D Fe-CH-75, (e,f) 2D Fe-CH-100, and (g,h) 2D Fe-CPA.

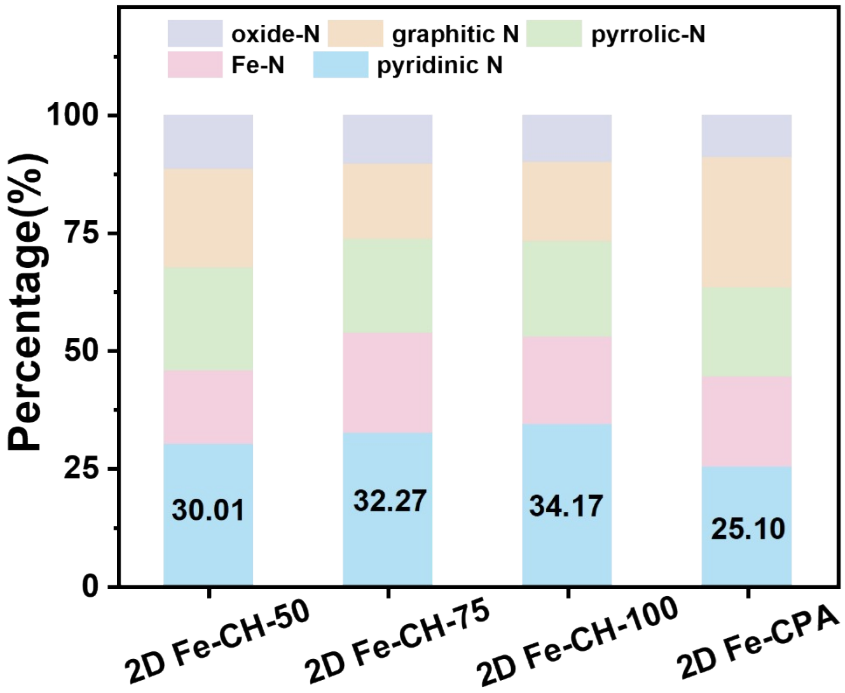

Fig. S10 N species fraction in 2D Fe-CH-50, 2D Fe-CH-75, 2D Fe-CH-100, and 2D Fe-CPA.

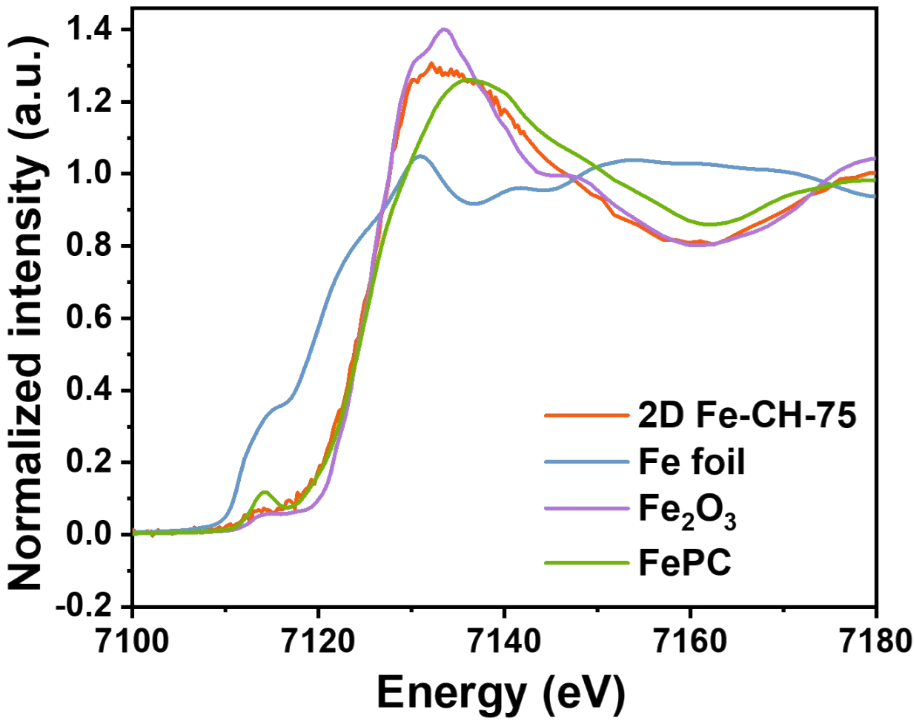

Fig. S11 Normalized Fe K-edge XANES spectra for 2D Fe-CH-75 and reference samples.

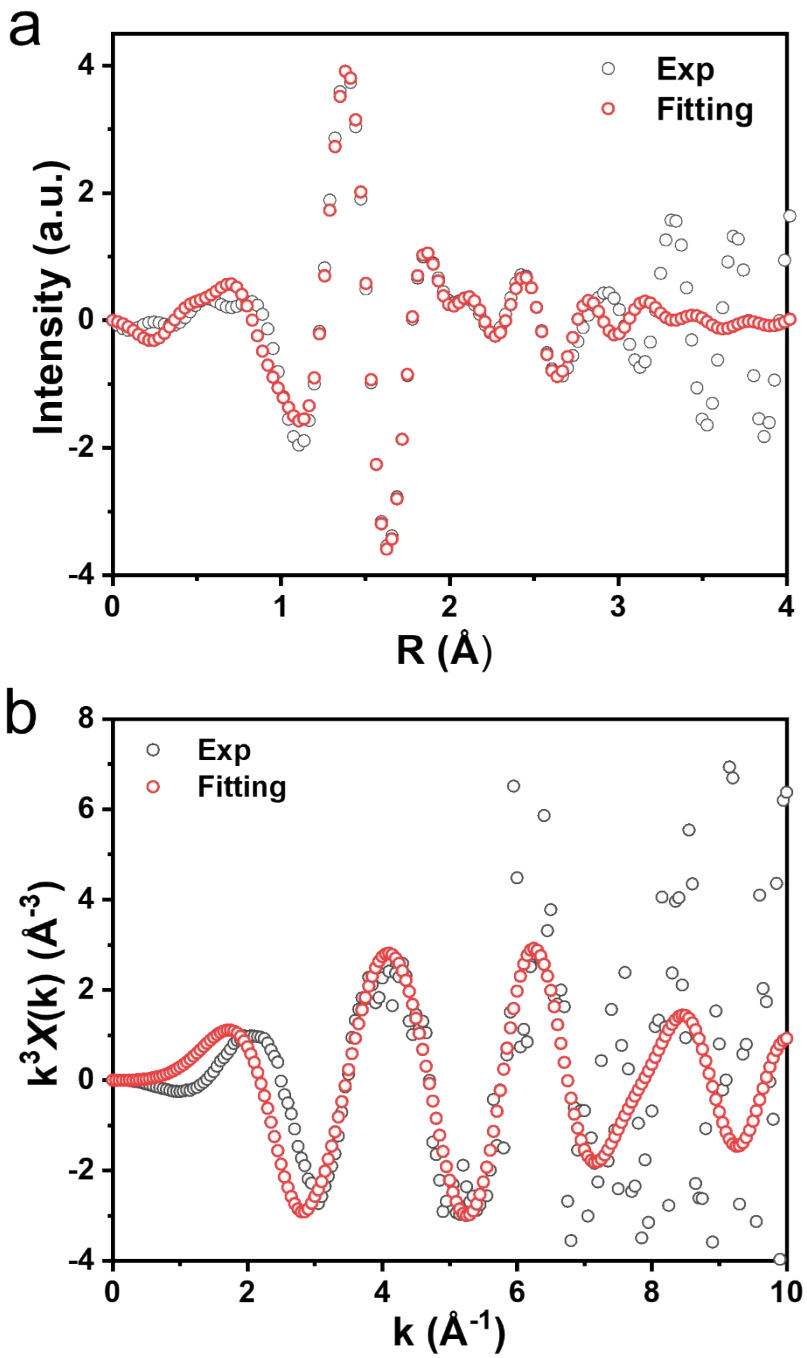

Fig. S12 FT-EXAFS spectra and corresponding fitting of Fe K-edge at (a) R-space and (b) k space.

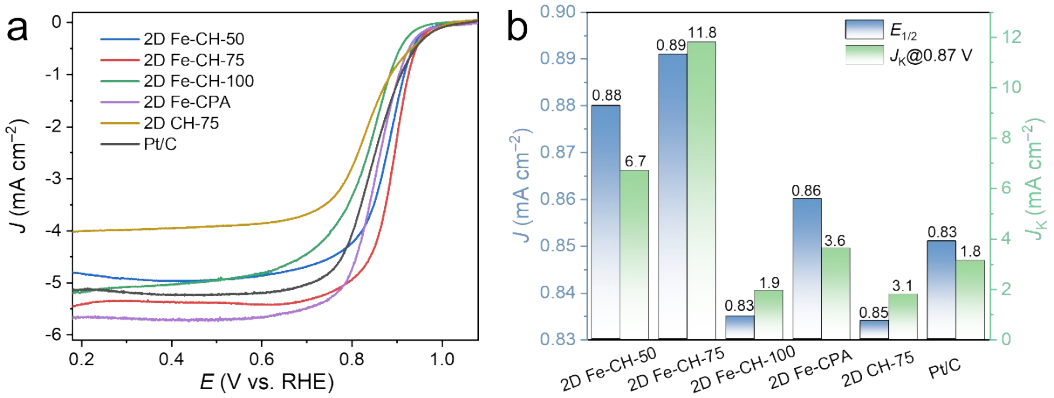

Fig. S13 (a) LSV curves and (b) half-wave potential and calculated J_k at 0.87V of 2D Fe-CH-50, 2D Fe-CH-75, 2D Fe-CH-100, 2D Fe-CPA, 2D CH-75, and commercial 20 wt% Pt/C.

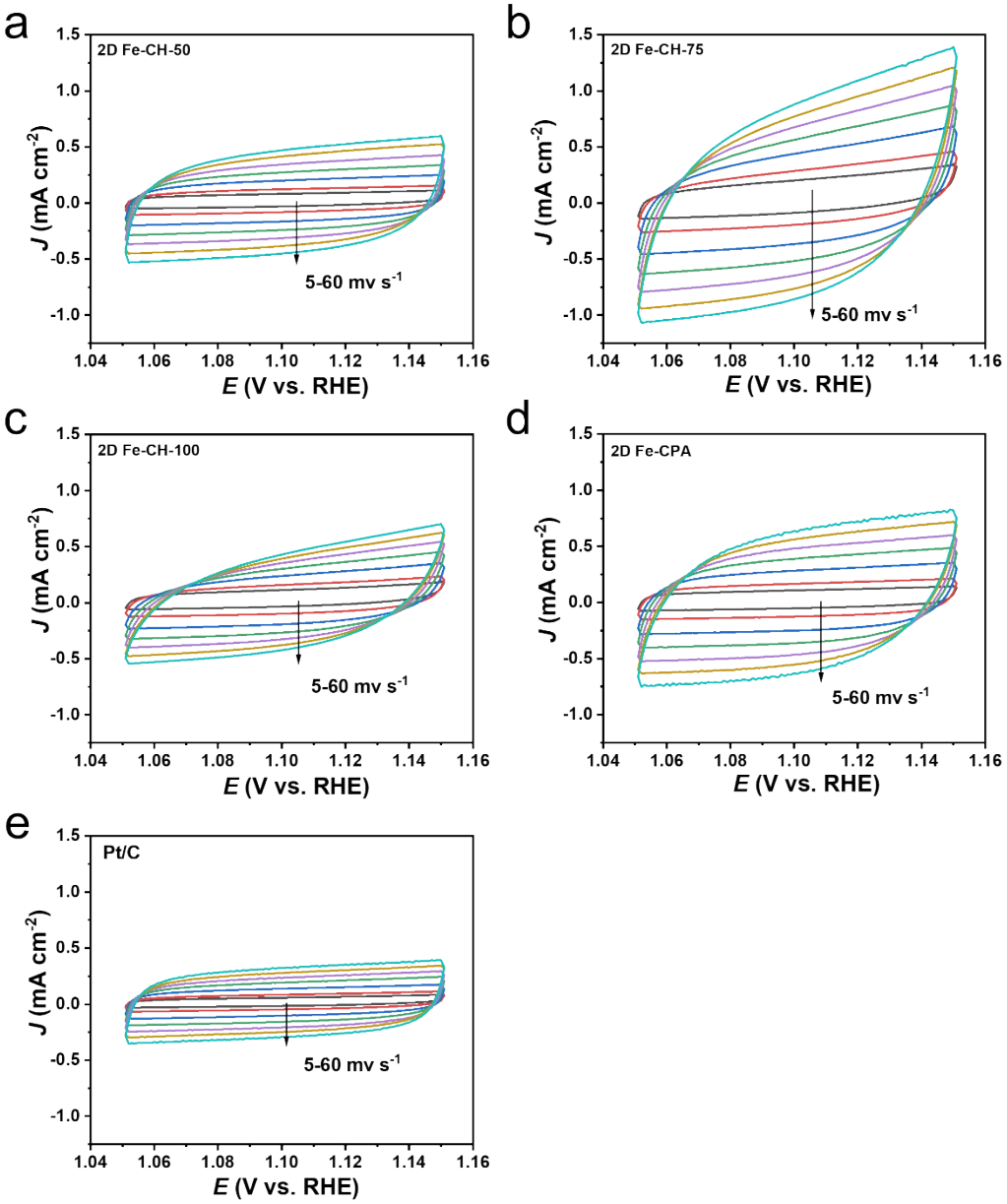

Fig. S14 The cyclic voltammograms curves in the non-faradaic region at different scan rates: (a) 2D Fe-CH-50, (b) 2D Fe-CH-75, (c) 2D Fe-CH-100, (d) 2D Fe-CPA, and (e) Pt/C.

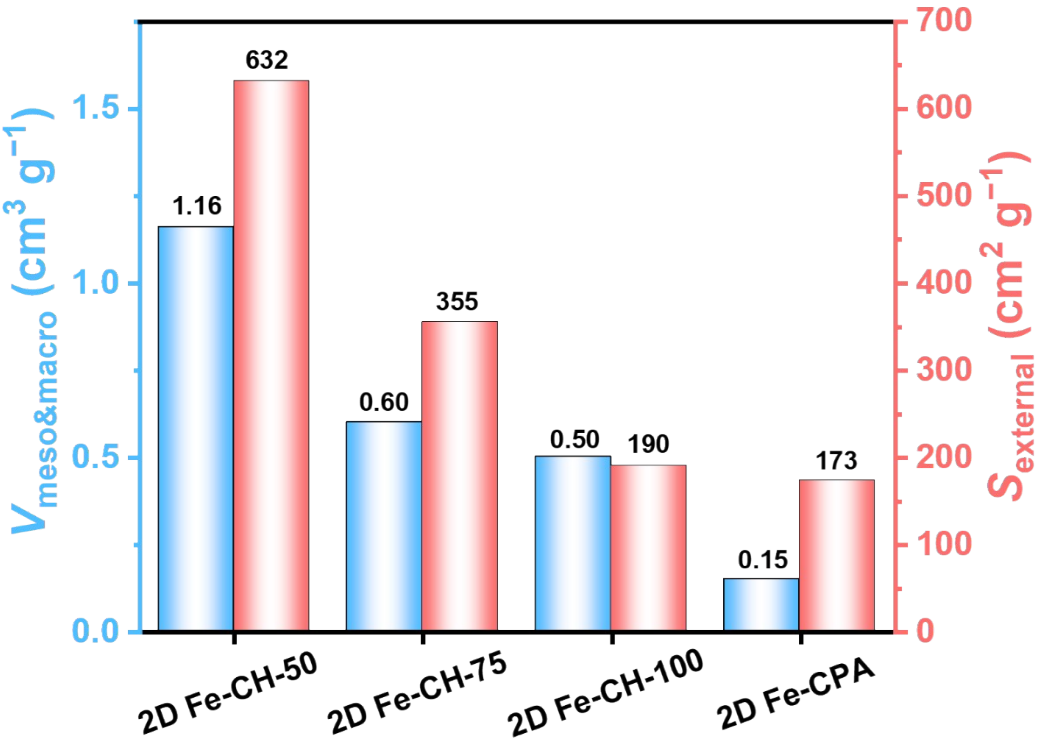

Fig. S15 The external surface area and meso- and macropore volume for 2D Fe-CH-50, 2D Fe-CH-75, 2D Fe-CH-100, and 2D Fe-CPA.

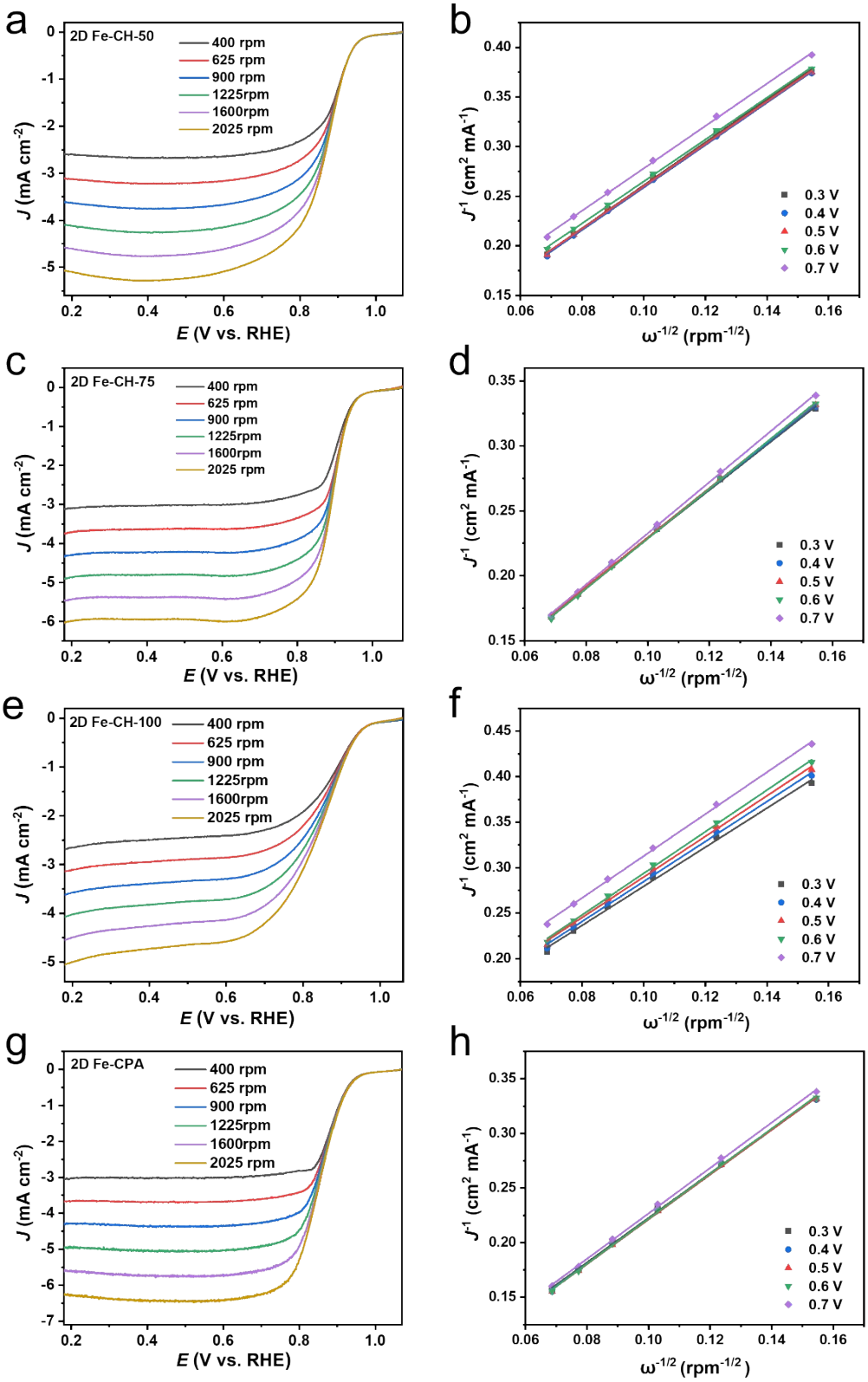

Fig. S16 Polarization curves with rotating speed from 400 to 2025 rpm and corresponding K-L plots of (a,b) 2D Fe-CH-50, (c,d) 2D Fe-CH-75, (e,f) 2D Fe-CH-100, and (g,h) 2D Fe-CPA.

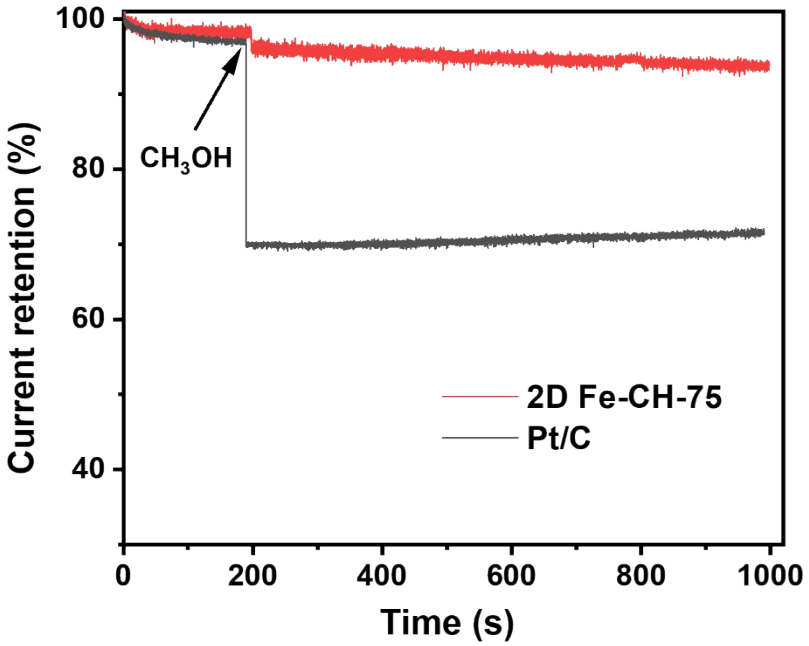

Fig. S17 Current retention from chronoamperometric curves of FeNCH-75 and 20 wt % Pt/C.

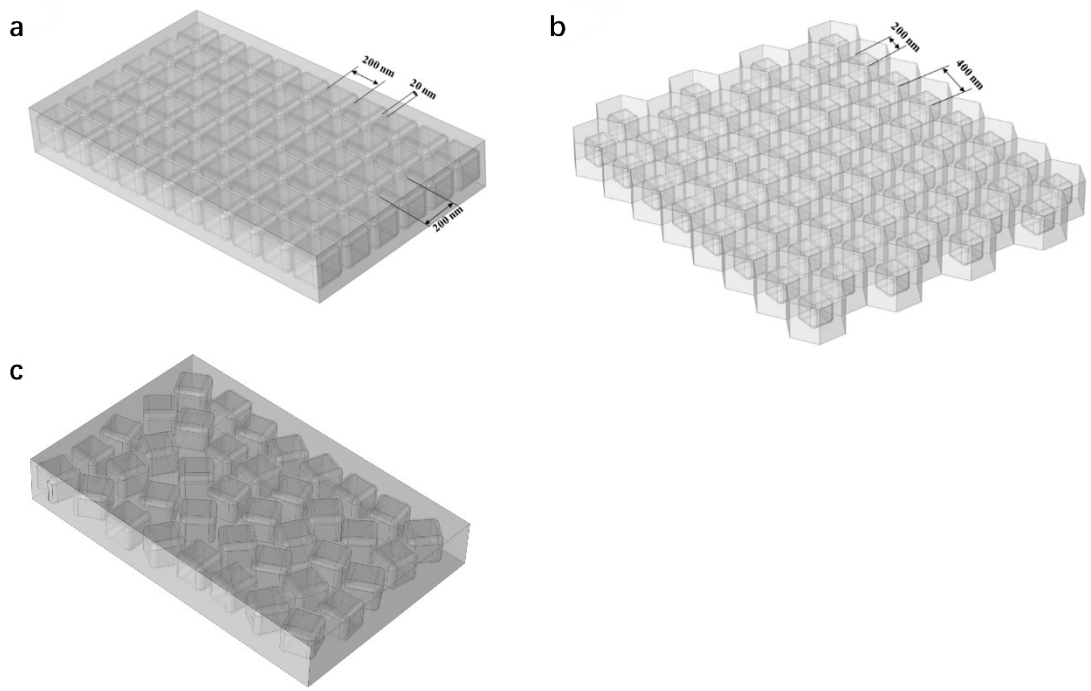

Fig. S18 Schematic description of three simulation models. (a) 2D ordered particle array model for 2D Fe-CPA, (b) confined 2D particle array with hexagonal lattices model for 2D Fe-CH-75, and (c) 2D disordered particle array model for 2D Fe-CPA.

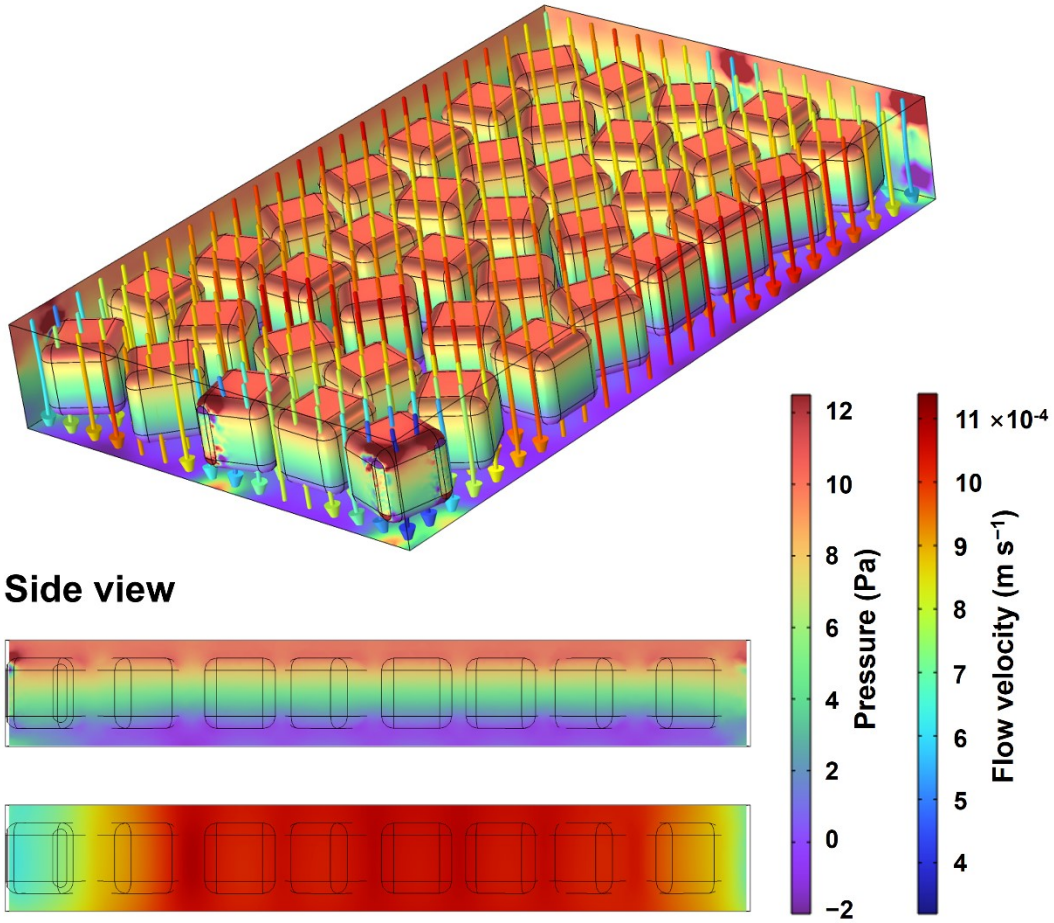

Fig. S19 Schematic description of 2D disordered particle array model for 2D Fe-CPA.

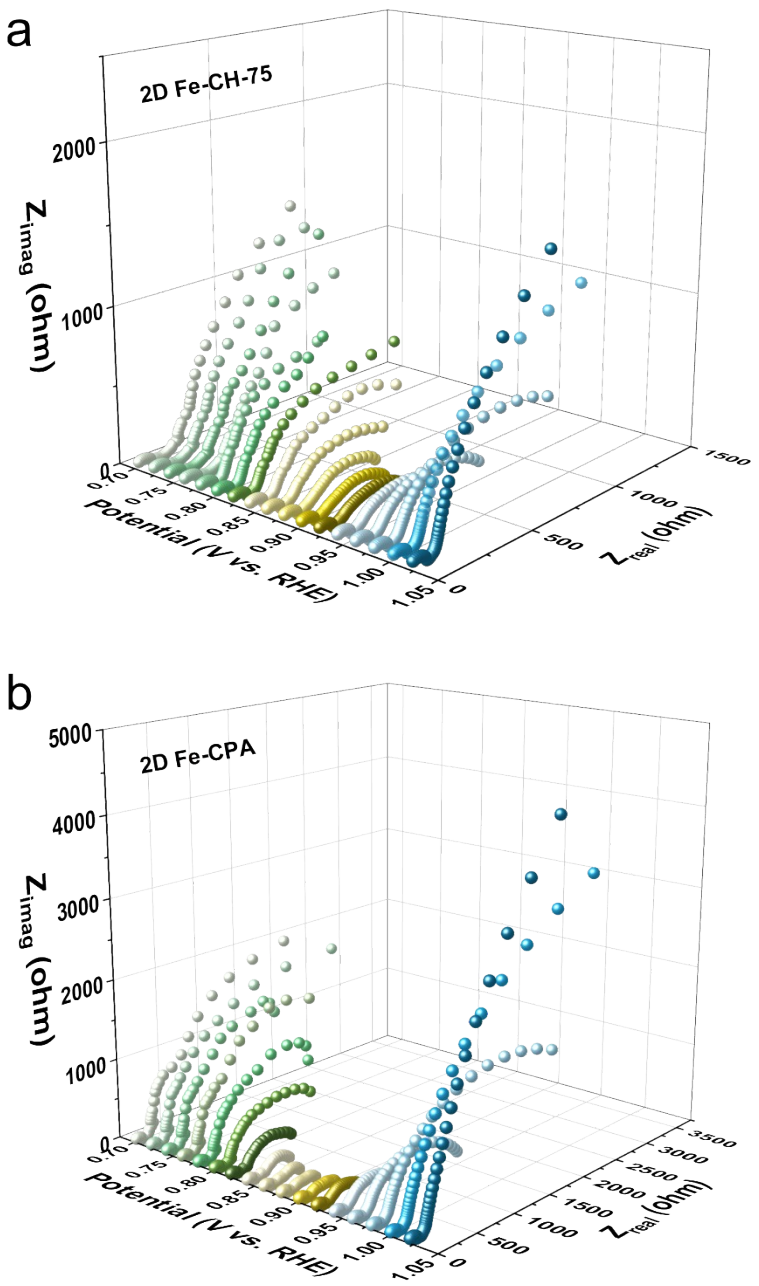

Fig. S20 Nyquist plot of in-situ EIS measurement of (a) 2D Fe-CH-75 and (b) 2D Fe-CPA.

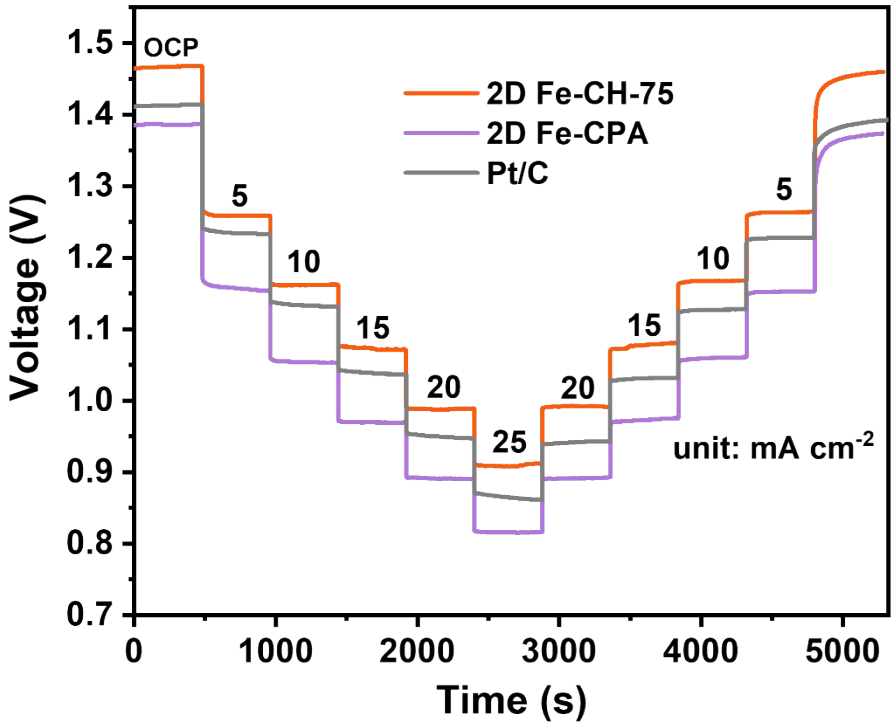

Fig. S21 Galvanostatic discharge curves of 2D Fe-CH-75-based and Pt/C-based Zn-air batteries at different current densities.

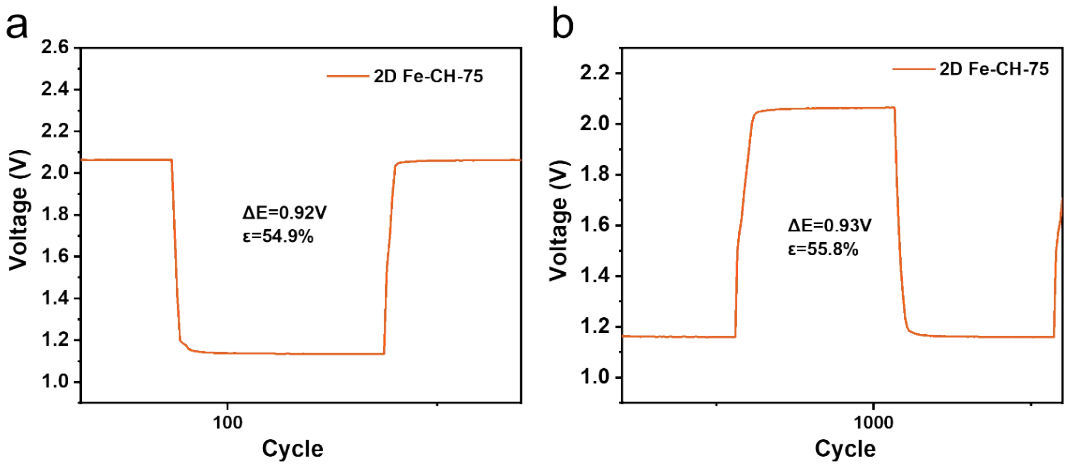

Fig. S22 (a) The 100th and (b) 1000th discharge/charge cycle curves of the liquid ZABs equipped with 2D Fe-CH-75+RuO_2 cathode (The charge and discharge plateau voltages used here are their average values).

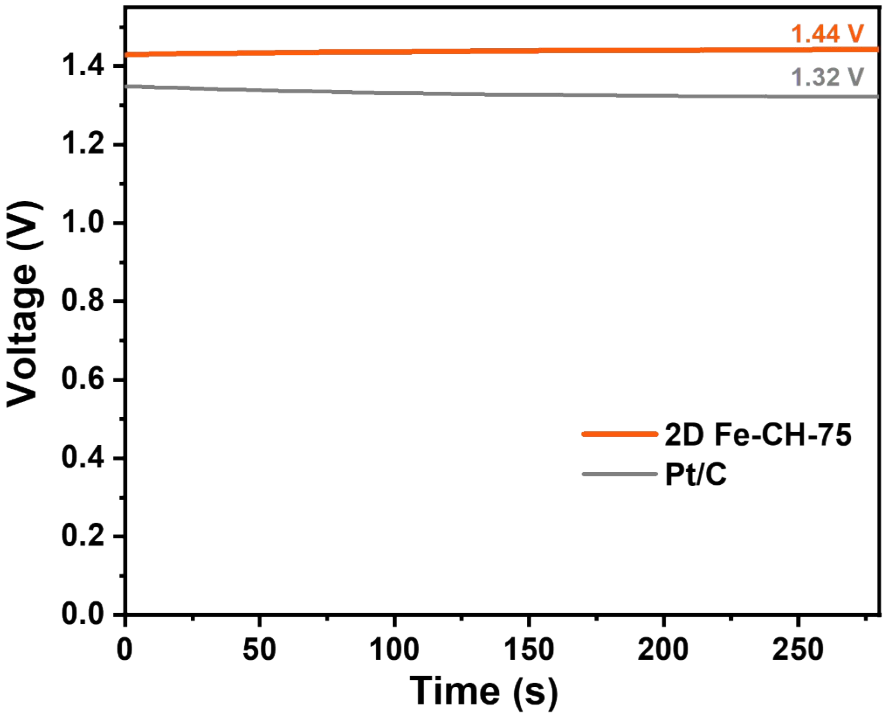

Fig. S23 Open circuit voltage curves of the flexible ZABs with 2D Fe-CH-75 and Pt/C.

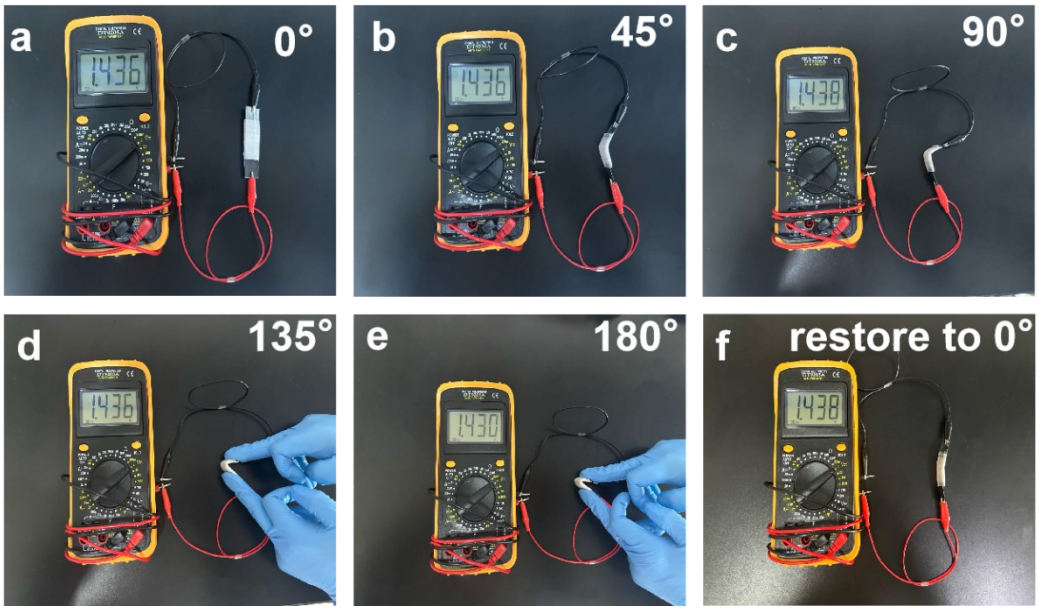

Fig. S24 The open circuit voltage of the flexible ZABs with 2D Fe-CH-75 cathode under different bending angles.

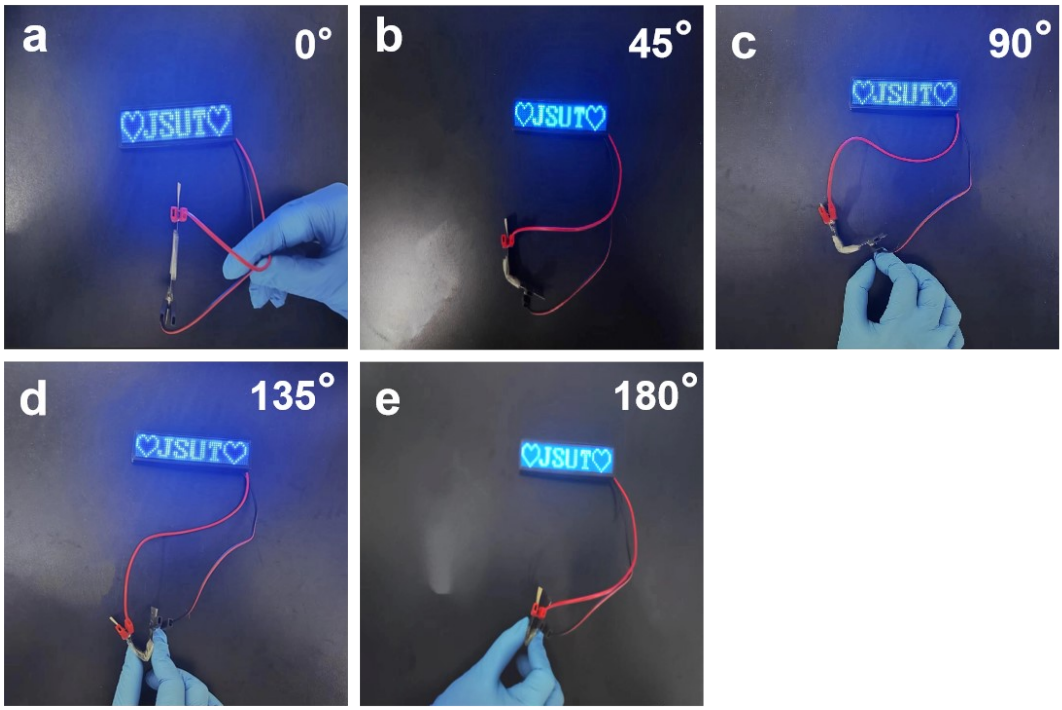

Fig. S25 The open circuit voltage of the flexible ZABs with 2D Fe-CH-75 cathode under different bending angles.

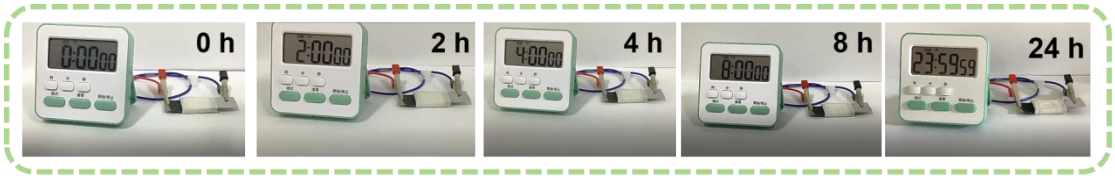

Fig. S26 The flexible battery assembled with 2D Fe-CH-75 powered the clock for 24 h.

Table S1. The BET surface area and the total pore volume of different samples.

Sample	Specific surface area S_{BET} ($m^2\ g^{-1}$)	Total pore volume V_{total} ($cm^3\ g^{-1}$)	Microporous surface area S_{micro} ($m^2\ g^{-1}$)	Microporous pore volume V_{micro} ($cm^3\ g^{-1}$)
2D Fe-CH-50	1338	1.46	706	0.30
2D Fe-CH-75	1121	0.92	766	0.32
2D Fe-CH-100	936	0.87	746	0.37
2D Fe-CPA	1278	0.60	1105	0.45

Table S2. Fe content determination values (F-AAS) and theoretical calculation values for 2D Fe-CH-*n* and 2D Fe-CPA catalysts.

Sample	Mass ration in Precursor ZIF-8: urea: Fe^{3+}	Mass of prepared catalyst from different batches (mg)				Calculated value (wt%)	F-AAS (wt%)
		1	2	3	4		
2D Fe-CH-50	300:50:2	20.0	18.5	24.5	19.7	1.98%	1.60%
2D Fe-CH-75	300:75:2	22.9	23.0	22.1	23.5	1.79%	1.23%
2D Fe-CH-100	300:100:2	26.9	27.8	26.8	27.0	1.49%	1.14%
2D Fe-CPA	300:0:2	21.3	21.4	20.0	21.6	1.90%	2.01%

Table S3. Comparison of ORR catalytic activity between 2D Fe-CH-75 and other previously reported single-atom ORR electrocatalysts in 0.1 M KOH.

Sample	Half-wave potential (V vs. RHE)	Tafel Slope (mV dec^{-1})	Ref.
2D Fe-CH-75	0.891	55.1	This work
Mn-N-C	0.89	78	*Angew. Chem. Int. Ed.* **2025**, 64, e202503934.
Fe/CoSx-SNC	0.885	86.35	*Chem. Eng.* J. **2024**, 502, 158080.
Re-NG	0.86	97	*CCS Chem*. **2025**, 7, 2508−2519.
Fe-CNG SACs	0.89	57	*Nat. Commun*. **2021**, 12, 55890
Se@NC-1000	0.85	52	*Angew. Chem. Int. Ed.* **2022**, 61, e202114441.
Co SAs/N-C	0.881	75	*Angew. Chem. Int. Ed.* **2016**, 56, 10800−10805.
CeNC-M-0.6	0.88	55.7	*Adv. Energy Mater*. **2025**, 15, 2404689.
SA-Fe-N_5	0.89	69.94	*ACS Nano.* **2025**, 19, 12161−12169.
Fe-1	0.882	82	*ACS Nano* **2022**, 16, 15994−16002.
Fe SA/NCZ	0.87	70	*Adv. Funct. Mater.* **2023**, 33, 2213897

Table S4. Comparison of ZABs performance between 2D Fe-CH-75 and other previously reported ORR electrocatalysts.

Sample	Open Voltage (V)	Peak Power Density (mW cm^{-2})	Ref.
2D Fe-CH-75	1.47	223.3	*this work*
Fe-MaPCS-100	1.48	157.5	*Adv. Funct. Mater.* **2026**, 36, e16222
Fe_2-NC-850	1.47	110.3	*J. Am. Chem. Soc.* **2025**, 147, 19210-19216
ZIF-Fe-NC	1.483	170.1	*ACS Sustainable Chem. Eng.* **2025**, 13, 333-342.
Fe-N-MESs	1.53	252.2	*Nano Res.* **2025**, 18, 94907886.
$FeZnCe_5$-NC	1.54	172.4	*Chem. Eng. J.* **2024**, 498, 155487
NiFe-LDH/Fe-N-C	1.54	205.0	*Adv. Energy Mater.* **2023**, 13, 2203609.
CoNP@FeNC-0.05	1.51	104.4	*Nano Micro Lett.* **2022**, 14, 162.
ZnCoNiCuFe@PCF	1.515	240.9	*ACS Nano* **2026**, 20, 5021-5033
FeDy-DAC	1.515	231.8	*Adv. Mater.* **2026**, n/a, e20359.
Fe_2NC-Cl	1.5	231	*J. Am. Chem. Soc.* **2026**, 148, 5167-5178.
FeMn-N-C	1.494	151	*Adv. Mater.* **2024**, 36, 2405763.